Journal of The Electrochemical Society

Influence of Particle Size and Mass Loading of Hard Carbon on Sodium Ion Battery Rate Performance in Industrially Relevant Full Cells

Journal of The Electrochemical Society, 2024 **171** 023506

Influence of Particle Size and Mass Loading of Hard Carbon on Sodium Ion Battery Rate Performance in Industrially Relevant Full Cells

Christopher Constable,[1,z] Fazlil Coowar,[2] Mark Copley,[1] Emma Kendrick,[3] Claire Dancer,[1] and Ivana Hasa[1,z]

[1]*WMG, University of Warwick, Coventry CV4 7AL, United Kingdom*
[2]*Faradion Limited, The Innovation Centre, Sheffield, S1 4DP, United Kingdom*
[3]*School of Metallurgy and Materials, University of Birmingham, Birmingham, United Kingdom*

Sodium-ion batteries (SIBs) represent a great opportunity for stationary storage, back-up power supply and light electric vehicle applications. Energy and power requirements for these applications needs to be satisfied. Beside material improvement, electrode microstructure plays a critical role. Herein, the influence of hard carbon (HC) particle size and mass loading on the rate performance have been comprehensively investigated. This work analyses the relative contribution of ionic resistance within the porous electrode (R_{ion}) in SIB full cells employing relevant mass loadings. R_{ion} was obtained by applying electrochemical impedance spectroscopy (EIS) to symmetrical cells and by fitting a transmission line model (TLM) under "*blocking*" conditions. The relative contribution of R_{ion} arising from HC electrodes was further compared to the charge transfer resistance (R_{CT}) in full cell configuration utilising a three-electrode cell under "*non-blocking*" conditions. Results illustrate mass loading to be as far more influential on cell rate performance compared to the two particle sizes analyzed. The three-electrode study reveals the contribution of R_{ion} to be greater than that of R_{CT} at high mass loadings and high states of charge for the HC electrode and elucidates that the gravimetric and volumetric discharge capacity of cells is limited by the layered oxide cathode and HC electrode respectively.
 [DOI: 10.1149/1945-7111/ad2590]

Manuscript submitted October 23, 2023; revised manuscript received January 9, 2024. Published February 23, 2024.

Supplementary material for this article is available online

Sodium ion batteries (SIBs) are regarded as one of the most promising future electrochemical energy storage systems.[1,2] Due to their potential lower cost, enhanced sustainability and improved safety compared to lithium-based chemistries, SIBs have a great opportunity to be utilised in future stationary storage applications including residential, industrial and remote location storage, back-up power supply and in low cost light electric vehicle applications.[3] To meet the desired specification for these applications, research surrounding improving electrode materials and manufacturing is required in order to enhance cell level energy and power density.[4]

The electrode microstructure and design contribute significantly to the rate capability and cycle life of the cell.[5] Key parameters for electrode design include the primary particle size (μm), particle shape, porosity (v/v%), inactive material content (binder and conductive additive) and areal loading (mg/cm^2) for both the positive and negative electrode. These parameters can be adjusted to create electrode microstructures for either high energy or high-power cells.

Typically, thinner electrodes result in greater power to energy ratio, however as a result, the cell level gravimetric energy density (Wh/kg) tends to be lower and cell cost higher. Alternatively, thicker electrodes tend to have a lower power to energy ratio but can lead in principle to devices which have higher cell-level gravimetric energy density. The second option certainly has some advantages, however obtaining high areal loading electrodes is not always an easy task from a manufacturing perspective and additional limitations are present in terms of cell performance. Therefore, as a result, modest loadings reflected in lower electrode thicknesses are often applied in commercialised cell design, even when energy density is desired.[5]

Indeed, previous studies on lithium-based chemistries suggest the decrease in rate performance associated with thick, high areal mass loaded electrodes (mg/cm^2) can be attributed to the resistance associated with electrolyte transport within the porous electrode (R_{ion}), the interfacial overpotential (η_-) at the negative electrode,[5] and the tortuosity (τ) related to the electrode microstructure. Whether these limiting factors are similar for sodium-based systems is so far relatively unexplored, particularly for industrially relevant electrode loadings, and full cell systems. Characterising R_{ion} is challenging as its contribution must be separated from other cell resistance contributions including the high frequency resistance (R_{HF}) attributed to the separator, electrolyte and cell housing components, the charge transfer resistance (R_{CT}) associated with the interface of the electrode and electrolyte, and the contact resistance (R_{cont}) associated with the interface between the cell's electrodes and current collectors.

One method to extract the relative contribution of cell resistances is via fitting an equivalent circuit model (ECM) to the alternating current (AC) impedance response of the cell. De Levie initially proposed a model of a cylindrical pore of semi-infinite length to describe the AC impedance response of porous electrodes in electrolytic solutions.[6] The work used a form of transmission line model (TLM) to describe this behaviour. Bisquert[7] further enhanced this model by proposing a generalised TLM expression. The generalised equation is formulated through description of current and potential distributions down a pore with cylindrical geometry in both the solid and liquid phases. Subsequently Ogihara et al.[8] proposed an analytical approach to determine the relative contributions of ionic resistance R_{ion}, charge transfer resistance R_{CT}, and solution resistance R_S in lithium ion battery (LIB) cathode material.

The methodology enabled the study of the impedance response of symmetrical cells where one electrode material is used for both electrodes within the cell. A TLM in "*blocking*" conditions was fitted to the impedance response, isolating R_{ion} contributions. Landesfeind et al.[9] further extended this method as a way to analytically determine the electrode tortuosity, and further suggested the use of blocking electrolyte and the use of a constant phase element (CPE) to model the interface when the cell is in "*blocking*" configuration. "*Blocking*" configuration refers to an electrode where charge transfer across the electrode interface is not feasible and thereby eliminated as a source of internal resistance. "Non-blocking" conditions on the other hand refer to conditions where charge transfer can occur, this type of TLM can be fitted to the impedance response of an electrode where charge transfer and intercalation can

[z]E-mail: chris.constable@warwick.ac.uk; ivana.hasa@warwick.ac.uk

occur, for instance in a conventional sodium ion battery cell versus hard carbon.

More recently Linsenmann et al.[10] used TLMs to compare (de) lithiation and (de)sodiation of hard carbon. They observed charge transfer resistances (R_{CT}) were around ten times larger during (de) sodiation compared to (de)lithiation dominant across all states of charge (SOC), however, this study utilised electrodes with low mass loading.

The influence of mass loading on R_{CT} has not been investigated for the (de)sodiation of full cells at higher mass loading, hence warrants an investigation. There are additional challenges associated specifically with experimental approaches adopted when studying sodium-ion battery materials. Indeed, current studies tend to be limited to electrodes presenting low loadings and high proportions of inactive materials in the electrode composition. In addition, many studies report on half-cell experiments using sodium metal as a counter electrode, which, while representing an ideally endless sodium inventory, is also associated with instability at the interface with the electrolyte.[11,12] Careful consideration of half-cell data should be given as overly optimistic capacity values can be obtained by using higher electrolyte volumes and an abundant sodium source (sodium metal counter electrode), but at the same time, a build-up of resistance at the counter electrode (more pronounced in half cells) may induce polarisation.[13]

Indeed, issues associated with half-cells include a build-up of a resistive interface between sodium metal and electrolyte which would not be present in a full cell experiment, and a disparity in the ratio of sodium in each electrode compared to full cell design.

In this work the effect of three hard carbon (HC) mass loadings and two different particle size on rate performance have been investigated. The resultant R_{ion} from each electrode has been characterised by fitting a TLM under "*blocking*" conditions to symmetrical cell. Values for R_{HF}, R_{cont} and R_{CT}, are then characterised via three-electrode configuration ($Na_{1-x}Ni_{1-x-y-z}Mg_xMn_yTi_zO_2$ cathode, hard carbon anode and sodium reference) at various states of charge by fitting a TLM under "*non-blocking*" conditions. The three-electrode cells were used to identify the electrode limiting both the gravimetric (mAh/g_{AM}) and volumetric capacity (mAh/cm^3_{AM}) during cell operation across a range of discharge rates. Additionally, the use of three-electrode cells allowed for the investigation into the relative contributions of R_{CT} and R_{ion} during operation. Through combined use of symmetrical and three-electrode cells the influence of the sodium reference has been accounted for. Electrodes in this study use an active material composition ⩾95 wt% for both positive and negative electrodes. Finally, this investigation uses increasing mass loadings of up to 13.5 mg cm^{-2}, resulting in areal capacities of ∼1.5, 2.5 and 3.2 mAh cm^{-2} at three electrode thicknesses. The highest mass loading would give distinct commercially competitive advantages in energy density if scaled to multilayer pouch cells. The analysis proposed here may be re-produced for other full cell systems to assess the performance of each electrode and highlight specific areas of commercial cell design for further development whether this be targeting interfacial stability, active material or electrolyte improvements.

Experimental

Electrode preparation and cell assembly.—*Faradion Ltd* supplied the positive electrodes consisting of a $Na_{1-x}Ni_{1-x-y-z}Mg_xMn_yTi_zO_2$ layered oxide active material (AM), polyvinylidene fluoride (PVDF, Solvay) binder and conductive additive mix.

The electrodes were manufactured utilising N-Methyl-2-pyrrolidone (NMP, *Sigma-Aldrich*) as a solvent and contain an excess of ⩾95 wt% active material on a dry basis according to Faradion's specification. The supplied cathodes utilised a 21 μm carbon coated aluminium foil as a current collector.

Hard carbon (HC) negative electrodes were manufactured using KURANODE^{TM} Type1 HC (d_{50} = 9 μm) and Type2 HC (d_{50} = 5 μm). Particle size distribution (PSD) of the Type1 (9 μm) and Type2 (5 μm) HC materials has been confirmed by using a Mastersizer 3000 (Malvern) laser diffraction type particle analyser using the Aero S dry powder dispersion attachment. Figure S1 confirms the PSD for the two materials, showing similar values to the manufacturer's specification, with d_{50} values of 9.01 μm ± 0.12 and 5.23 μm ± 0.008 for Type1 and Type2 HC respectively.

A water-based processing method was used to prepare the HC electrodes by mixing the active material and combining with sodium carboxymethyl cellulose (CMC, Ashland) and styrene-butadiene rubber (SBR, Zeon) as binder, along with conductive additive TIMCAL SUPER C65 (C65, Imerys). Electrodes contain an active material percentage ⩾95 wt% on a dry basis according to Faradion's specification. Initially, CMC is mixed with water using a planetary mixer (Thinky ARE-250, intertronics, US) for 15 min at 1500 rpm, adding incrementally to ensure dispersion. The active material and conductive additive powders were pre-mixed dry and were added before further mixing for 30 min at 2000 rpm. Finally, SBR is added before a final mix for 10 min at 1000 rpm.

The HC slurry was then coated onto 15 μm thick aluminium foil, using a four-way applicator (Erichsen, Germany) targeting low, medium, and high loadings of 5.5 mg cm^{-2}, 9.5 mg cm^{-2} and 12.9 mg cm^{-2}. Electrode loadings were targeted based on providing an excess of hard carbon. This was calculated from the supplied cathode loadings between 8.20 mg cm^{-2} and 19.1 mg cm^{-2}. Electrode coatings were then dried under ambient temperatures (21 ± 2 °C) and transferred in a dry room (T_{DP} = −42 °C, < 50 ppmH_2O) where they were, calendered at 4000 psi by using a roll type calender (Innovative Machine Corp, US) to reach a target electrode density. The target density for anode and cathode coatings was kept consistent across all thicknesses of electrode.

After calendaring, 18 mm and 15 mm electrode disk were subsequently punched from the three coatings for the three-electrode (non-blocking) and symmetrical (blocking) cells respectively. Each electrode was weighed (Sartorius, ±0.1 mg) and measured for thickness (Mitutoyo, Japan, ±0.001 mm) to determine electrode mass loading. These measurements were used to select appropriately balanced electrodes for the three-electrode configuration. After weighing and measuring for thickness the electrodes are transferred to a glass drying oven at 120 °C (Buchi Kugelrohr B-585 with drying accessory) for ∼12 h under dynamic vacuum. After vacuum drying, electrodes were airlessly transferred to an argon filled glovebox (M-Braun, <0.5 ppm O_2, <1.0 ppm H_2O), where cells were assembled. Specific electrode formulation and full cell balancing details are not reported due to company restriction, however this does not limit understanding of the study carried out and the conclusions made from the final results.

Symmetrical cells (blocking conditions).—Symmetrical cells were constructed by placing electrodes in CR2032 coin cells (Type1 HC vs Type1 HC, Type2 HC vs Type2 HC and $Na_{1-x}Ni_{1-x-y-z}Mg_xMn_yTi_zO_2$ vs $Na_{1-x}Ni_{1-x-y-z}Mg_xMn_yTi_zO_2$ see Table I for cell configurations). The coin cell set-up utilised 1 × 1 mm spacer in a conventional configuration, applying 70 μl (∼40 μl cm^{-2}) of 1 M $NaPF_6$ in EC:DEC (3/7 v/v%) + 2 wt% FEC (*Fluorochem Ltd*) electrolyte. Once cells had been sealed, they were placed in a BH-1i cell holder (Biologic Inc.) and transferred to a temperature-controlled chamber at 25 °C (BINDER) before connecting to a VMP-3 type potentiostat (Biologic Inc.).

Three-electrode cells (non-blocking conditions).—Three-electrode cells were assembled using the EL-Cell PAT-cells with PAT-core insulation sleeve. The PAT-core used in the current set of experiments uses the Freudenberg Viledon FS 2226E and Lydall Solupor 5P09B (PP) separator and a ring type sodium reference electrode (part no. ECC1–00–0210-X/X). The 250 μm plunger was used in the PAT core for this series of cells. 1 M $NaPF_6$ in EC:DEC (3/7 v/v%) + 2 wt% FEC (*Fluorochem Ltd*) was used as the electrolyte, with 100 μl used per cell (∼ 41 μl cm^{-2}). All parts of the assembly were dried for at least 12 h at 60 °C prior to introduction to the glovebox and cell system. Once cells were

Table I. Symmetrical two- and three-electrode cell test configurations.

Test	Cell form factor	Electrode 1	Electrode 2	Reference electrode
T1	3-Electrode PAT Cell	KURANODE™ Type1 (9 um)	$Na_{1-x}Ni_{1-x-y-z}Mg_xMn_yTi_zO_2$	Yes—Na ring ref
T2	3-Electrode PAT Cell			Yes—Na ring ref
T3	3-Electrode PAT Cell			Yes—Na ring ref
T4	3-Electrode PAT Cell	KURANODE™ Type2 (5 um)	$Na_{1-x}Ni_{1-x-y-z}Mg_xMn_yTi_zO_2$	Yes—Na ring ref
T5	3-Electrode PAT Cell			Yes—Na ring ref
T6	3-Electrode PAT Cell			Yes—Na ring ref
T7	CR2032 Symmetrical Cell	KURANODE™ Type1 (9 um)	KURANODE™ Type1 (9 um)	No
T8	CR2032 Symmetrical Cell			No
T9	CR2032 Symmetrical Cell			No
T10	CR2032 Symmetrical Cell	KURANODE™ Type2 (5 um)	KURANODE™ Type2 (5 um)	No
T11	CR2032 Symmetrical Cell			No
T12	CR2032 Symmetrical Cell			No
T13	CR2032 Symmetrical Cell	$Na_{1-x}Ni_{1-x-y-z}Mg_xMn_yTi_zO_2$	$Na_{1-x}Ni_{1-x-y-z}Mg_xMn_yTi_zO_2$	No
T14	CR2032 Symmetrical Cell			No
T15	CR2032 Symmetrical Cell			No

sealed, they were transferred to 2 × 4-channel PAT stand (EL-CELL, Germany) and placed inside a temperature-controlled chamber at 25 °C (BINDER) and connected to a VMP-3 type potentiostat (Biologic Inc.).

Electrochemical analysis.— *Symmetrical cells (blocking conditions).*—The potentiostatic electrochemical impedance spectroscopy (PEIS) program was used under open circuit potential. A frequency range between 200 kHz-0.5 Hz was selected with a potential perturbation of 20 mV. Ten measurements per decade were taken with a 0.1 period spacing between each measurement averaging two readings per frequency. As fresh electrodes were used the state of charge (SOC) of the symmetrical cell is equivalent to 0%.

Three-electrode testing (non-blocking conditions).—Faradion's layered oxide ($Na_{1-x}Ni_{1-x-y-z}Mg_xMn_yTi_zO_2$) constituted the working electrode (denoted by WE subscript) and the HC (Type1 or Type2) electrode constitutes the counter electrode (denoted by CE subscript). The reference electrode is a ring type sodium reference located in-plane with the separator of the cell. The electrochemical test procedure has three sections: (1) 5 full cycles at C/10 (1 C = 130 mA/g_{AM}), (2) a rate test upon discharge from C/5 to 10 C (3) nine cycles at C/10 followed by galvanostatic electrochemical impedance spectroscopy (GEIS) measurement at four states of charge (SOC) upon charge and five SOC upon discharge (see Fig. S2 for overview of part 3 test procedure).

The initial cycling protocol consisted of 5 cycles at C/10, utilising a constant current (CC) followed by a constant voltage (CV) step upon charge (CC = C/10 till [E_{WE} - E_{CE}] ⩾ 4.2 V then CV until the current falls < C/20 or 20 h). Discharge is conducted at C/10 until [E_{WE} - E_{CE}] ⩽ 1.0 V. E_{CE} vs Na/Na^+ is measured during all procedures allowing comparison of each electrode's contribution towards the total cell potential.

Rate tests involved a similar procedure to the described initial cycling, this time with 3 cycles CC charge at C/5 until upper cut-off voltage is reached ([E_{WE} - E_{CE}] > 4.2 V). Discharge is CC at varying C-rates (C/5, C/2, 1 C, 2 C, 3 C, 5 C, 7 C, and 10 C), with three cycles at each rate.

The EIS tests at different SOC study were performed on cells formed at C/10 using the CCCV mode described above for 9 cycles. Prior to charging (on the 10th cycle) an initial adaptive amplitude galvanostatic EIS (GEIS-AA) measurement was taken. The cell was then subsequently charged at C/10 to four SOCs at which point EIS measurements were conducted after a cell rest period of one hour (E_{cell} = 1.0 V, 1.8 V, 2.6 V, 3.4 V and 4.2 V). Due to the expected voltage decay upon opening the circuit (OCV) the actual potential varied slightly from the defined cut off (see Table S3 for full breakdown of potential levels tested). The cell was then discharged at constant current, with GEIS-AA performed at the same potentials upon discharge. Z_{CE} vs Na/Na^+ was also measured during GEIS-AA measurements allowing for the isolation of the counter electrode's impedance response. For the GEIS-AA measurement a frequency range between 200 kHz-0.5 Hz was applied with the adaptive amplitude option targeting a 20 mV perturbation. The 20 mV perturbation was targeted as this still gave a linear response as determined through calculating residuals whilst also reducing noise. Ten measurements per decade were taken with a 0.1 period spacing between each measurement averaging two measurements per frequency. The GEIS-AA was used due to a non-compatibility issue between the GCPL6 technique and PEIS measurement. GEIS/PEIS spectra were tested for linearity using the Lin-KK tool which applied the Kramers-Kronig transform[14–16] (see Fig. S5 for summary data).

EIS data from symmetrical two- and three-electrode cells were exported to Schreiber Zview software for fitting of an equivalent circuit model (ECM). TLM representation was achieved using Bisquert #2[17] equivalent circuit under the extended element options, this allows for both modelling the "*blocking*" conditions in the symmetrical cell and "*non-blocking*" conditions in the three-electrode configuration. Fitting was achieved using a maximum of one hundred iterations, using the Calc-Modulus data weighting option. R_{ion} values were divided by two at the end of fitting to assign the value of ionic resistance per electrode for the symmetrical cell configuration.

Results and Discussion

In order to understand the limiting factors determining rate performance in the investigated sodium-ion cells, impedance spectroscopy has been carried out. To better understand the contributions arising from the anode and the cathode independently, EIS measurements were conducted on *i)* symmetric two electrode coin cells under blocking conditions and *ii)* three-electrode cells consisting of a working electrode, a counter electrode, and a Na reference electrode, which allowed individual determination of the impedance of the positive and negative electrodes.

Figure 1 illustrates the TLM in the frequency domain using a set of arbitrary values to model "*blocking*" and "*non-blocking*" conditions. A useful simplification for initial estimation of R_{ion} is to consider the 45° mid-frequency region of the Nyquist plot. The length of the 45° region equates to $R_{ion}/3$ when a TLM under "*blocking*" conditions is applied.[7] To ensure comparability between the different test types the resistances and capacitances are multiplied and divided by the electrode's cross-sectional area respectively.

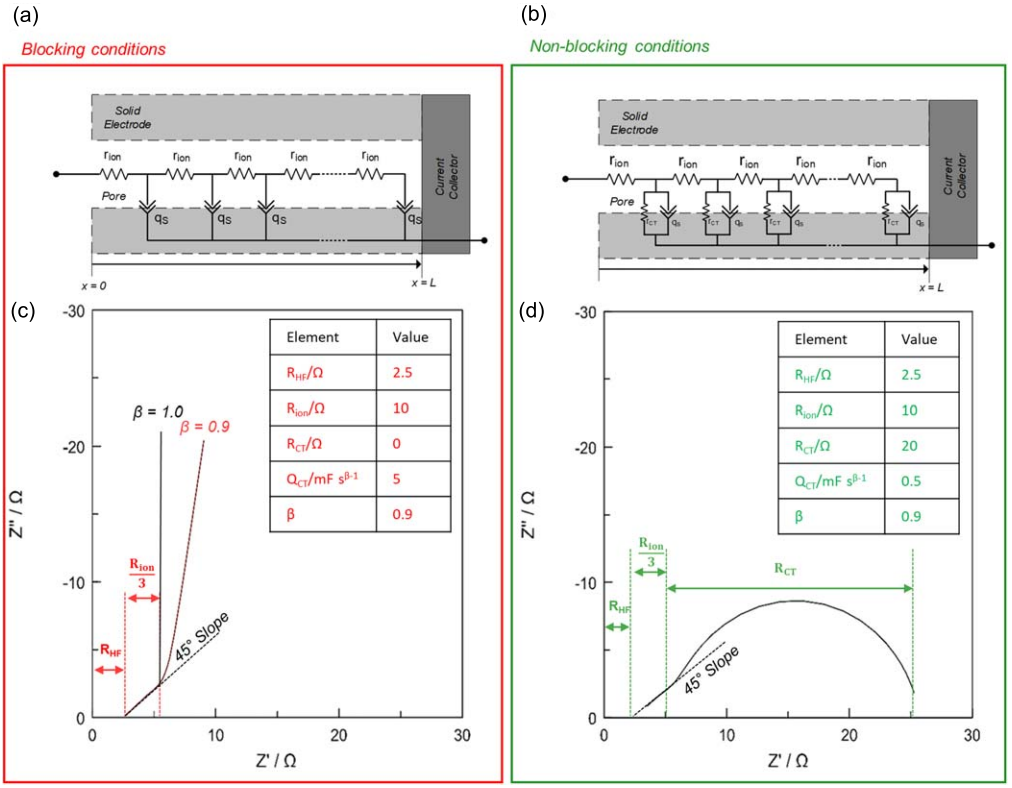

Figure 1. The grey schematics represents the inner region ($0 < x < L$) of a porous electrode as defined by the transmission line model (TLM) consisting of a porous film deposited on a conducting substrate. The schematic shows configurations under (a) "*blocking conditions*" and (b) "*non-blocking conditions*." (c) The Nyquist Plot for non-ideally polarisable "*blocking*" conditions (used to fit symmetrical cell impedance response), illustrating the distinctive dog legged response given by Eq. 1. (d) The Nyquist Plot under non-ideally polarisable "*non-blocking*" conditions (used to fit Z_{CE} vs Na/Na^+ three-electrode data), illustrating the mid to low frequency charge transfer resistance semi-circle given by Eq. 2. Figure has been adapted from Bisquert.[7]

Symmetrical cell testing—blocking conditions.—The Nyquist plots of the symmetrical cells is reported in Fig. 2.

The Nyquist plots of the HC symmetrical cells (Figs. 2a, 2b) exhibit a high frequency resistance (R_{HF}) representing the sum of the ionic resistance of the electrolyte filled separator and the electronic resistance of external cell contacts. This is followed by a 45° region at intermediate frequencies and finally a constant phase type element at low frequencies, indicated by a near vertical line[18] (see Fig. 1a for breakdown of impedance response). The response of the porous cathode in symmetrical cells, reported in Fig. 2c is instead characterised by a high frequency resistance (R_{HF}), followed by the contact resistance between the porous electrode and the current collector (R_{Cont}) visualised as a semicircle, a 45° region and a final contribution associated with the constant phase element (CPE). Data were fitted and the corresponding fitting results are reported in Table II.

The first thing to consider in the response is the high frequency resistance, R_{HF}. This varied from 5.6–6.7 Ωcm^2 for the hard carbon electrode types and 5.6–7.0 Ωcm^2 for the $Na_{1-x}Ni_{1-x-y-z}Mg_xMn_yTi_zO_2$ cathode. Following the high frequency resistance, the 45° region is associated with the ionic resistance within the electrode pore space, R_{ion}. The data reveal an increase in the R_{ion} value with increasing electrode mass loadings, indicated by a lengthening of the 45° region of the Nyquist plot (see Figs. 2a–2c). For the Type1 HC (9 μm) the value of ionic resistance increased from 17.1 Ωcm^2 at an electrode loading of 4.6 mg cm^{-2} to a value of 43.4 Ωcm^2 at a loading of 12.6 mg cm^{-2}, suggesting an increase proportional to the thickness of the electrode. In a similar vein, the Type2 HC (5 μm) exhibited an increase in R_{ion} value from 15.7 Ωcm^2 at a loading of 5.2 mg cm^{-2}, to 32.0 Ωcm^2 at a loading of 13.6 mg cm^{-2}. The increase in R_{ion} is marginally lower than the values observed with the Type1 HC (9 μm).

It is worth mentioning that when performing initial investigations, a slight deviation from the 45° phase angle in both symmetrical and three-electrode cells was observed suggesting the addition of an R/Q element into the equivalent circuit. Equation 1 describes the impedance response for the symmetrical cell with the additional R/Q element:

$$Z = R_{HF} + \frac{R_{cont}}{1 + R_{cont}C_{cont}j\omega} + \sqrt{\frac{R_{ion}}{Q_S(j\omega)^{\beta}}}\coth\left(\sqrt{R_{ion}Q_S(j\omega)^{\beta}}\right) \quad [1]$$

This behaviour has been observed in previous studies and is thought to be a result of the contact resistance at higher frequencies either arising between the electrode and the current collector or the separator.[18,19] In some equivalent circuits, the CPE exponent is fixed at one, thus reducing the CPE element to a capacitive element. Despite the observed variation contact resistance values for both Type 1 and Type 2 remain low (0.56–1.14 Ωcm^2) relative to the ionic and high frequency resistances. There is an increase of the surface CPE "capacitance" Q_S, visually seen in the third region of the Nyquist plot (see Fig. 1/2). This result suggests the blocking conditions are followed with increasing mass loadings.

Interestingly, the layered oxide cathode showed no obvious trend in R_{ion} value with increasing mass loadings. For the layered oxide cathode, the R_{ion} values decreased from 13.17 Ωcm^2 at an electrode loading of 11.1 mg cm^{-2} to 10.5 Ωcm^2 for a loading of 18.0 mg cm^{-2} (see Fig. 2c). Similarly to the HC electrodes, the value of Q_S increases linearly with thickness, with CPE capacitance here being around twice that obtained in the HC electrodes. R_{cont} and C_{cont} values for the layered oxide symmetrical cells also have larger contributions evident in the high frequency semi-circle observed in the Nyquist plot (see Fig. 2c). Despite the visual prominence of the semi-circle, the influence of the contact resistance remains small

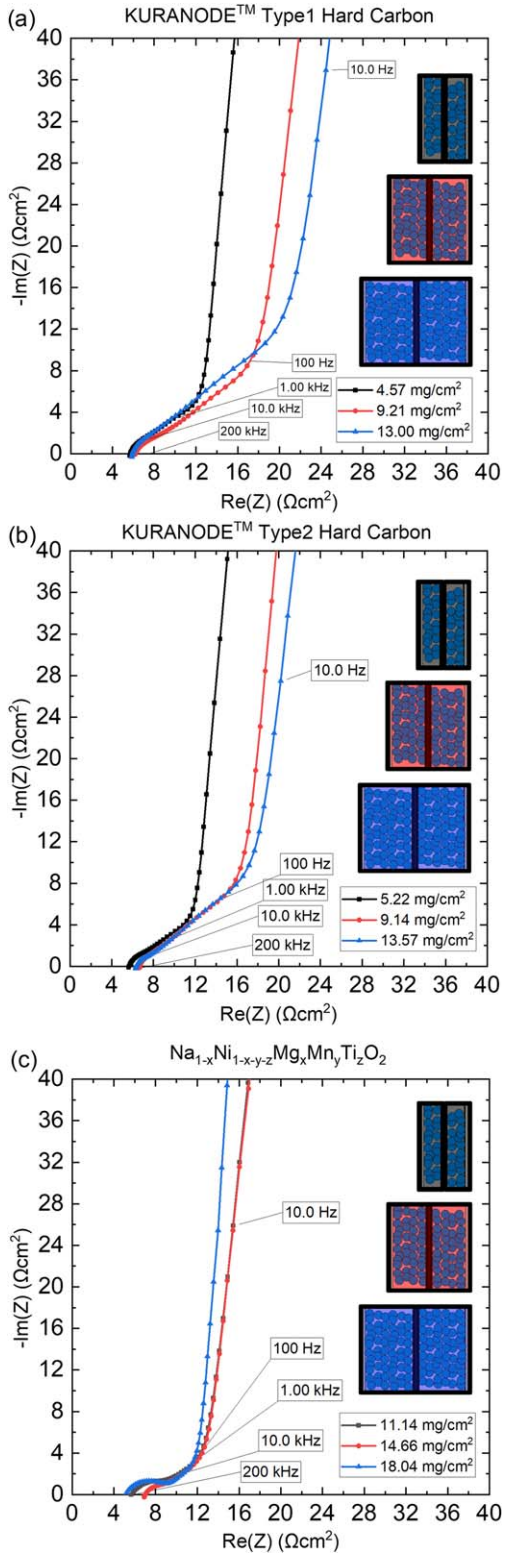

Figure 2. Nyquist plots of (a) KURANODE™ Type1 HC [9 μm] (b) Type2 HC [5 μm], and (c) $Na_{1-x}Ni_{1-x-y-z}Mg_xMn_yTi_zO_2$ symmetrical cells at low (black), mid (red) and high mass loadings (blue). Captions refer to the frequency (Hz) of the applied potential perturbation and are shown each decade. Notice an increase in the 45° region with mass loading for hard carbon materials compared to a small increase registered in the cathode material. These mass loadings correspond to mass loadings used in the three-electrode full cells used in Fig. 3.

when compared to ionic resistances in the layered oxide (see Table II). The small influence of mass loading on the R_{ion} value in the symmetrical cell containing the layered oxide material may be due to the smaller thickness arising due to the higher density of the material relative to the hard carbon material. Indeed, considering the intrinsic differences in density ($\sim$0.9 g cm^{-3} for hard carbon and $\sim$2.8 g cm^{-3} for the cathode) it is clear that an increase in mass loading at the cathode does not translate to the same increase of thickness that the anode experiences when increasing the loading, suggesting that the thickness variation exhibited by the cathode may not be sufficient to induce strong effects on R_{ion}. However, further studies in this regard are required to further clarify the trend.

The potential inability of the sodium layered oxide to reach "*blocking*" conditions, which were assumed in the fitting of the blocking TLM, may also be responsible of the results. While the use of a non-intercalating salt may ensure "*blocking*" conditions as reported by Landesfeind et al.,[9] an intercalation salt was used in this study as this has been used successfully in previous investigations by Ogihara[20] and is more representative of full cell conditions. Additionally, there is some difficulty in differentiating the regions between the high frequency contact resistance and the 45° region associated with the ionic resistance which could again contribute to this result. After accounting for the two electrodes' contribution, the data become comparable to those obtained by Linsenmann et al.[10] when extrapolating the linear trend of ionic resistance with mass loading down to the levels used in their study (3.0 mg cm^{-2}).

At low frequency, all impedance spectra exhibited a steep sloping line, typical of the CPE element. There is some debate about whether to model the interface as a capacitive element (i.e. $\zeta = 1/q_s j\omega$) as originally proposed by Ogihara et al.,[20] or to model the interface as CPE as presented by Landesfeind et al.[9] ($\zeta = 1/q_s[j\omega]^{\beta}$). The reason for a non-ideal capacitance within a cell under blocking conditions remains unclear, however, theories have been proposed to explain why this behaviour may arise. Mulder et al. suggest this behaviour might arise due to the fractal nature of surface roughness within the sample.[21] Other suggestions include non-uniform reaction rates,[22] anomalous diffusion[23] or a non-uniform current distribution.[24] For this work the CPE was used to model the interface under "*blocking*" conditions and an R/Q element used for "*non-blocking*" conditions as it is characteristic of the low frequency response detected (see Figs. 2a–2c). Standard liquid electrolyte was used in this study as curvature of the impedance response at low frequencies were not observed under "*blocking*" conditions as seen in some studies.[9] The use of similar electrolyte between symmetrical and full cell systems allowed a more direct comparison of resistance values obtained from fitting symmetric to three-electrode cells as opposed to using a specialist blocking electrolyte in the symmetrical cell configuration.

Three-electrode testing—non-blocking conditions.—Above we presented a two-electrode symmetrical cell where charge transfer resistance, R_{CT}, was removed by imparting "*blocking conditions*" allowing elucidation of the changes in ionic resistance, R_{ion}. The ionic resistance of the anode increased with electrode thickness, on the other hand hard carbon particle size showed minimal influence on R_{ion} values at comparable mass loadings. In this section, the effect of individual electrodes is extracted by using three-electrodes cells. This allows for the comparison of ionic resistance within the electrode's pores, R_{ion}, to be compared to the charge transfer resistance, R_{CT}, at various states of charge. An R/Q element was added to the ECM used to model the counter electrode in the three-electrode configuration under "*non-blocking conditions*," making the final fitting equation:

$$Z = R_{HF} + \frac{R_{cont}}{1 + R_{cont}Q_{cont}(j\omega)^{\beta cont}} + \sqrt{\frac{R_{ion}R_{CT}}{1 + R_{CT}Q_{CT}(j\omega)^{\beta}}}\coth\left(\sqrt{\frac{R_{ion}}{R_{CT}}}\sqrt{1 + R_{CT}Q_{CT}(j\omega)^{\beta}}\right) \quad [2]$$

Table II. EIS fitting values for R_{HF}, R_{cont}, R_{ion} and Q_S, obtained from symmetrical cells under blocking condition. Values are referred to the full symmetrical cell response.

Material	Loading level	R_{HF} (Ωcm^2)	R_{cont} (Ωcm^2)	Q_{cont} (mF $s^{(\beta cont-1)}/cm^2$)	β_{cont} (-)	R_{ion} (Ωcm^2)	Q_S (mF $s^{(\beta-1)}/cm^2$)	β_S (-)
$Na_{1-x}Ni_{1-x-y-z}Mg_xMn_yTi_zO_2$	Low Loading | 11.1 mg/cm^2	5.80	2.48	0.07	0.76	13.17	0.80	0.93
	Mid Loading | 14.4 mg cm^{-2}	7.02	1.38	0.13	0.77	12.84	1.02	0.93
	High Loading | 18.0 mg/cm^2	5.31	3.15	0.04	0.77	10.51	1.46	0.95
KURANODE™ Type1 Hard Carbon (9 μm)	Low Loading | 4.6 mg cm^{-2}	5.51	1.05	0.033	1.0	17.13	0.220	0.94
	Mid Loading | 9.2 mg cm^{-2}	6.23	1.14	0.016	1.0	30.11	0.433	0.92
	High Loading | 12.6 mg cm^{-2}	5.54	0.66	0.075	1.0	43.40	0.598	0.92
KURANODE™ Type2 Hard Carbon (5 μm)	Low Loading | 5.2 mg cm^{-2}	5.54	0.82	0.025	1.0	15.68	0.276	0.94
	Mid Loading | 9.6 mg cm^{-2}	6.44	0.54	0.061	1.0	27.73	0.476	0.94
	High Loading | 13.6 mg cm^{-2}	6.30	0.56	0.026	1.0	31.99	0.782	0.93

The electrochemical performance of the investigated sodium-ion cells with different electrode mass loading is reported in Fig. 3.

Figures 3a, 3b report the first cycle losses (FCL) for full cells containing Type1 and Type2 HC respectively. The HC anodes are matched to the cathode material and are balanced at the same ratio of active material. Figure 3c illustrates areal capacity for the six full cell tests showing distinct areal capacities at the three mass loading levels across the 5 initial cycles conducted at C/10. The initial cycling steps at C/10 produced capacities in the range of 120 mAh g^{-1} to 130 mAh g^{-1} (with respect to the cathode) after five cycles, with lower loaded electrodes reaching the upper end of this range. First cycle losses for the electrode material increased slightly across the three mass loadings tested between 13% and 16% for Type1 cells and 16% to 17% for cells containing Type2 (see Figs. 3a, 3b). The variation in capacity can therefore be explained by the utilisation of sodium within the cell, with lower loadings utilising a marginally larger proportion of available sodium.

The rate performance of cells obtained by matching different electrode loadings has been investigated in three-electrode cell configuration. The cell potential of each electrode was monitored via the sodium reference (Na/Na^+) electrode to deconvolute the potential response of the full cell and thereby determine which electrode contributed to rate limitation. Figures 4 and 5 illustrate the potential response of the working electrode (sodium layered oxide cathode, E_{WE} *vs* Na/Na^+) and counter electrode (HC, E_{CE} *vs* Na/Na^+), at low (C/5) and high (10 C) rates across the four corners of the experimental design during cell discharge. E_{WE} and E_{CE} traces have been normalised to the mass of active material within their respective electrodes (i.e., sodium layered oxide and hard carbon respectively) in Fig. 4 and to their respective volumes in Fig. 5.

Figure 4a illustrates the response of the full cell where Type1 HC is used at a low loading level of 5.0 mg cm^{-2}. The solid blue line indicates the potential profile of the sodium layered oxide cathode and the solid red line the potential of Type1 HC at a low discharge rate of C/5. The difference between these traces represents the full cell potential ($E_{CELL} = E_{WE} - E_{CE}$). As we are interested in mass limitation within the cell, the potential profile of each electrode is normalised relative to the mass of active material contained within that specific electrode (i.e., mAh/$g_{cathode}$ for E_{WE} vs Na/Na^+ and mAh/g_{anode} for E_{CE} vs Na/Na^+, summarised by mAh/g_{AM} on axis, AM = active material). The blue solid trace (cathode at low rate) in Fig. 4a can be seen as limiting as it decreases from 4.2 V to 2.1 V ($\Delta V = 2.1$ V) compared to Type1 HC (solid red line) going from 0.1 V to 1.1 V ($\Delta V = 1.0$ V). The working electrode's potential (cathode) drops faster at high rates (dashed line) relative to the rise in potential exhibited by the Type1 HC, mirroring the trend at lower discharge rates. The other variable tested in this design is the mass loading of working and counter electrode. Figure 4b shows the capacities achieved when the mass loading of Type1 HC was increased to 12.4 mg cm^{-2} (the working electrode mass loading is also increased to keep the full cell active material mass ratio constant). Relative to the lower loading in Fig. 4a the specific capacity achieved by the working electrode at C/5 drops from 120 mAh/$g_{cathode}$ to 109 mAh/$g_{cathode}$ and the counter electrode capacity falls from 236 mAh/g_{anode} to 162 mAh/g_{anode}. The drop in value reflects the influence of mass loading on capacity even at the low discharge rate of C/5. Interestingly the capacity achieved from HC in full cell configuration is significantly smaller than what is observed in conventional half-cell configuration (250–330 mAh/g_{anode}).[10]

This can be explained considering that in half-cell tests, an abundant sodium inventory is guaranteed by using a sodium metal counter electrode, which generally leads to higher capacities. In addition, while the N/P ratio may also play a role, it is worth mentioning also that the "low" loadings employed in this study, i.e., 5 mg cm^{-2}, are much higher compared to loadings generally reported in literature (typically 1–3 mg cm^{-2}) for half- cell results,[25–28] thus potentially affecting the delivered capacity.

At the higher loading level depicted in Fig. 4b a greater drop off in capacity between the discharge rate of C/5 (solid line) and 10 C (dashed line) is observed. Figure 4c displays the capacities of working and counter electrode produced by Type2 (5 μm) hard carbon. The trend here is comparable to Type1 (9 μm) and the trend at high mass loading in panel Fig. 4d further illustrates comparable performance of Type2 HC (5 μm) at a high mass loading of 13.4 mg cm^{-2}. The full set of panels in Figs. 4a–4d clearly associate full cell gravimetric capacity limitations with the sodium layered oxide cathode.

Another important consideration is on the volumetric capacity (mAh/cm^3), as this is another metric on which to judge cell performance, and the identification of thelimiting electrode. Figure 5 shows volumetric discharge capacity normalised relatively to the volume of each electrode. Figure 5a exhibits the full cell response where Type1 HC is used at a low loading level of

5.0 mg cm^{-2}. The working electrode in this instance shows exceptional capacity of 328 mAh $cm^{-3}_{cathode}$, compared to the HC counter electrode achieving 181 mAh cm^{-3}_{anode}. The Type1 HC electrode is clearly limiting at low discharge rates of C/5 (indicated by the solid lines) and the trend of HC limitation still holds at discharge rates of 10 C as indicated by the dashed line. This limitation becomes obvious when considering the relative density of each active material, with hard carbon exhibiting a density of $\sim$0.9 g cm^{-3} relative to the sodium layered oxides exhibiting an electrode density of $\sim$2.8 g cm^{-3}.

Figure 5b shows the potential profiles for a three-electrode cell containing Type1 HC at the high mass loading of 12.4 mg cm^{-2}. The capacity of the sodium layered oxide drops from 261 mAh $cm^{-3}_{cathode}$ to 59 mAh $cm^{-3}_{cathode}$ and the capacity of Type1 HC decreases from 140 mAh cm^{-3}_{anode} to 32 mAh cm^{-3}_{anode} at 10 C, a significant decrease with the increased mass loading. Again, at the higher mass loading depicted in Fig. 5b a reduction in capacity retention is observed when compared to the lower mass loading level. The Type1 HC is limiting the volumetric discharge capacity at low (C/5) and high (10 C) discharge rates. Figure 5c displays the contributions to full cell potential from the full cells containing Type2 HC at a low loading of 6.1 mg cm^{-2}. There seems to be little influence on the capacities exhibited relative to the same loading of Type1 HC in Fig. 5a, and therefore deemed to have little influence on cell level performance. Figure 5d shows the Type2 HC containing three-electrode cell at the high mass loading of 13.4 mg cm^{-2}. Interestingly in this instance the cell becomes limited by the Type2 HC counter electrode at high discharge rate (10 C), as indicated by the dashed line. This is the one instance where the cathode becomes limiting on a volumetric capacity basis.

The rate capability across all discharge rates was assessed to consider the relative performance of the three mass loadings and two particle sizes. Figure 6 summarises the achieved capacity across the range of rates tested. The results have been normalised based upon the sodium layered oxide for the gravimetric capacity graph (Fig. 6a) and the hard carbon electrode for the volumetric capacity graph (Fig. 6b) as these were deemed limiting as shown in Figs. 4 and 5. This figure clearly shows mass loading as far more influential on rate capability in comparison to the particle size for the range of loadings (5.0–13.4 mg cm^{-2}) and HC particle sizes (9 μm and 5 μm) tested, confirming the observations made in the cathode and anode voltage profiles in Figs. 4 and 5. The slightly higher first cycle loss exhibited by Type2 HC (17%) can explain the marginally lower capacity achieved at low charge rates (C/5) in Fig. 6a.

The limited impact on performance of the different particle size at the anode may be associated to the length scale of the electrode (thickness). Particle size effects attributable to differences between 5 μm and 9 μm may only become influential when electrode thickness is on a similar length scale, e.g., 10 μm to 20 μm. The electrode thickness in these experiments is much greater than this and ranged from 62 μm to 155 μm, making the particle size to electrode depth ratio small. An interesting further investigation would be to test electrodes with a large particle size to electrode depth ratio, where particle size effects may become more influential. However, work on thinner electrodes is out of the scope of this work as the main goal was to investigate the mass loading influence on the rate performance of commercially relevant electrodes. Another possibility to improve rate performance could be to reduce the particle size further for the mass loadings tested within this study. It is worth noting though that reducing particle size considerably could lead to greater losses of capacity through increased first cycle losses, as confirmed in part by observations in this study (13%–16% for Type1 9 μm particles and 16%–17% for Type2 5 μm particles). A study by Bläubaum et al. has found particle size decrease until d_{50} = 1.5 μm to be beneficial, below this level particle size decrease negatively impacts rate performance.[29]

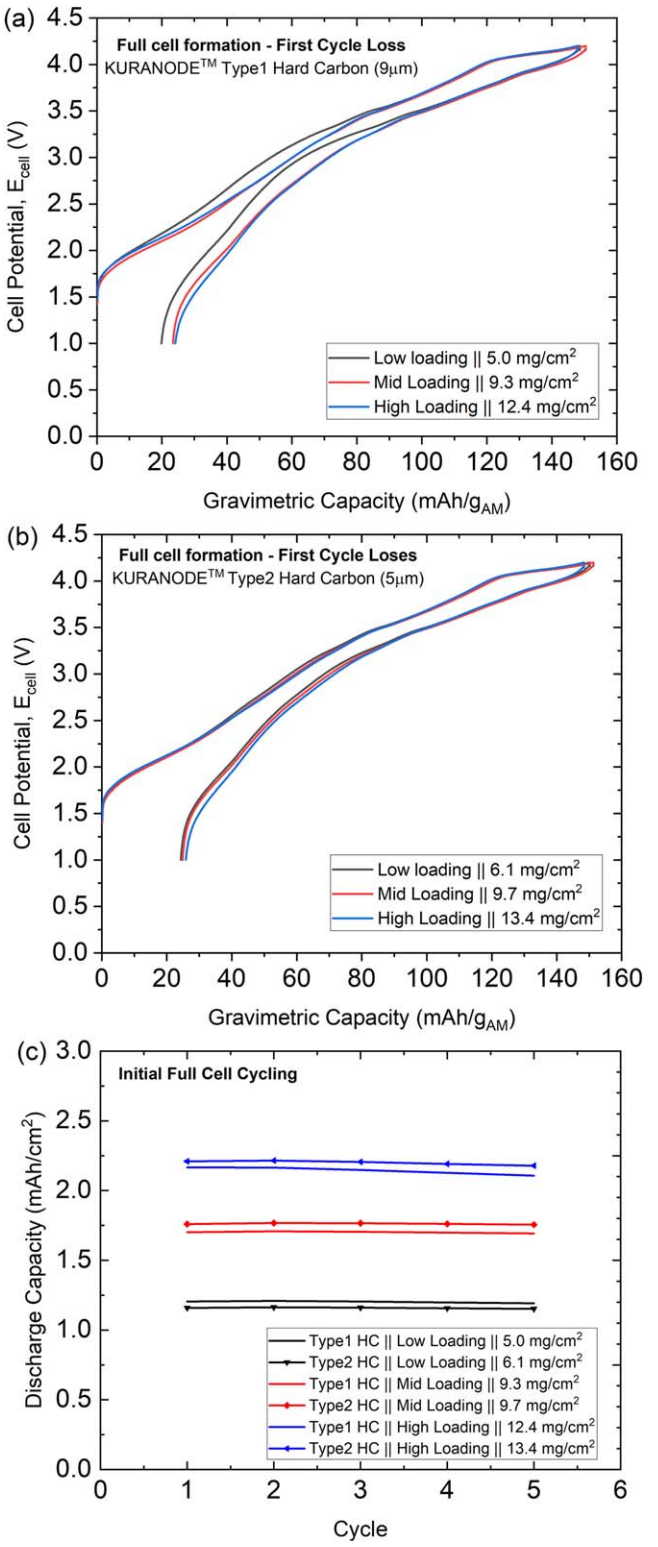

Figure 3. Voltage profiles ($E_{CELL} = E_{WE}–E_{CE}$) and cycling trend over the initial cycles for three-electrode full cells with different electrode mass loadings. (a) First charge/discharge cycle showing comparable first cycle losses across the three Type1 HC mass loadings tested, (b) first charge/discharge cycle showing comparable first cycle losses across the three Type2 mass loadings tested, and (c) discharge capacity vs initial cycle number confirming distinct areal discharge capacity across the three mass loading levels.

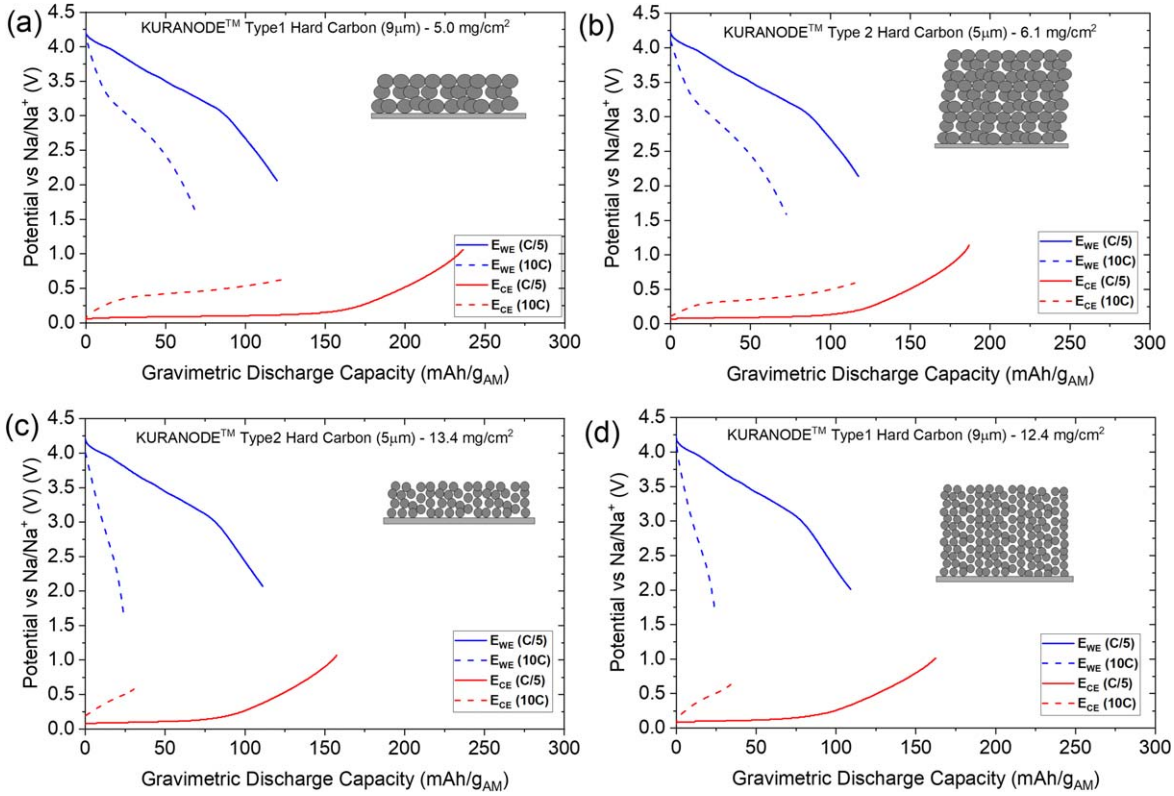

Figure 4. E_{CE} vs Na/Na^+ (hard carbon anode in red), and E_{WE} vs Na/Na^+ ($Na_{1-x}Ni_{1-x-y-z}Mg_xMn_yTi_zO_2$ layered oxide cathode in blue) vs gravimetric discharge capacity. Capacity is given per gram of the respective active material (i.e., per gram of hard carbon material for E_{CE} vs Na/Na^+, and per gram of sodium layered oxide material for E_{WE} vs Na/Na^+, denoted by g_{AM}). Solid and dashed lines represent cells at low and high discharging rates respectively (C/5 and 10 C, where 1 C = 130 mA/g_{cath}). These cells correspond to the four corners of the experimental design.

To understand the differences in the observed rate performance, EIS at different states of charge has been performed on cells containing different anode materials at different mass loadings in three-electrode format. EIS testing resulted in similar impedance responses at similar SOC upon charge and discharge (e.g., comparing GEIS-8 with GEIS-12 in Fig. S2), therefore the fitting of the equivalent circuit model was performed on EIS spectra captured during discharge. The potentials values at which the measurements correspond to SOC values ranging from 20.50% to 96.50% is shown in Fig. S2/Table S3 reporting a summary of the impedance measurements points.

Figure 7 reveals the various contributions towards the overall impedance arising from R_{HF}, R_{Cont}, R_{ion} and R_{CT} as a function of SOC for the three mass loading types and two HC particle sizes. These values are obtained through fitting to Eq. 2, detailed above.

At the low loading level reported in Figs. 7a, 7d (~5.5 mg cm^{-2}) the charge transfer resistance R_{CT} remained dominant resistance across all SOCs, in line with the previous finding by Linsenmann et al.[10] R_{CT} increases via a power law relationship with decreasing state of charge (power varies in range 2 to 3) across all loading levels. Figures 7b, 7e displays the mid-level mass loading (~9.5 mg cm^{-2}) where $R_{ion} > R_{CT}$ at SOC > ~60%. At the high mass loading of 12.4 mg cm^{-2} we see $R_{ion} > R_{CT}$ at SOC > ~50%, as illustrated in Figs. 7c, 7f. This trend is similar across both hard carbon types and fits in line with the expectation with increasing SOC. R_{cont} and R_{HF} remain mostly constant across the mass loadings and particle sizes tested. Small variations may be attributable to variation in the fitting of the TLM under non-blocking conditions, non-ideal behaviour associated with non-blocking conditions, or due to variations of the microstructure due to the build-up of solid electrolyte interphase (SEI). A build-up of SEI could cause changes to the microstructure and therefore cause variations in the value of R_{ion} across the SOC range. In the high loading Type1 electrodes R_{cont} becomes negligibly small so is removed from the fitting in this one instance. There is generally good agreement between values of R_{ion} reported between hard carbon in symmetrical cells and three-electrode full cells with the values corresponding to 17.13 Ωcm^2 and 14.84 Ωcm^2 at the low loading level and 43.40 Ωcm^2 and 46.83 Ωcm^2 at the high mass loading level. This shows good consistency between values obtained in the various test conducted.

Figure 8 reports the responses exhibited at low and high mass loadings for Type1 and Type2 HC counter electrodes. At low frequency (<5 Hz) the spectra exhibit a secondary depression of the semi-circle for both particle sizes at high electrode mass loading (13.4 mg cm^{-2} and 12.4 mg cm^{-2} respectively, see Figs. 8b, 8d). Interestingly there is a form of the TLM which considers this behaviour as originally presented in the works of Bisquert.[7] The behaviour can arise because of a non-zero current at the end of the pore. This may suggest an alternative reaction is taking place at the boundary, however further investigation is required to confirm such phenomena. It is worth noting that the potential of this electrode, E_{CE} never goes below 0 V vs Na/Na^+, therefore this side reaction is unlikely to be because of the onset of sodium plating which has been suggested in other studies[30] (Fig. 4 shows E_{CE} vs reference remaining above zero at full state of charge).

Further distortions at high and low frequency ranges were also observed which were challenging to fit. These features tended to be small in magnitude when compared to the overall impedance response (see Table S1/S2 for fitting values). Other studies have observed deviation in experiments away from the ideal TLM in the mid to high frequency region and associated with the 45° slope. Shodiev et al., suggested that this may be due to characteristic times at which porosity throughout the electrode is accessed as a function of frequency.[31] The deviation may also arise due to some contribution from the charge transfer resistance at similar frequencies. Cooper et al. used simulations to model the impedance spectra of

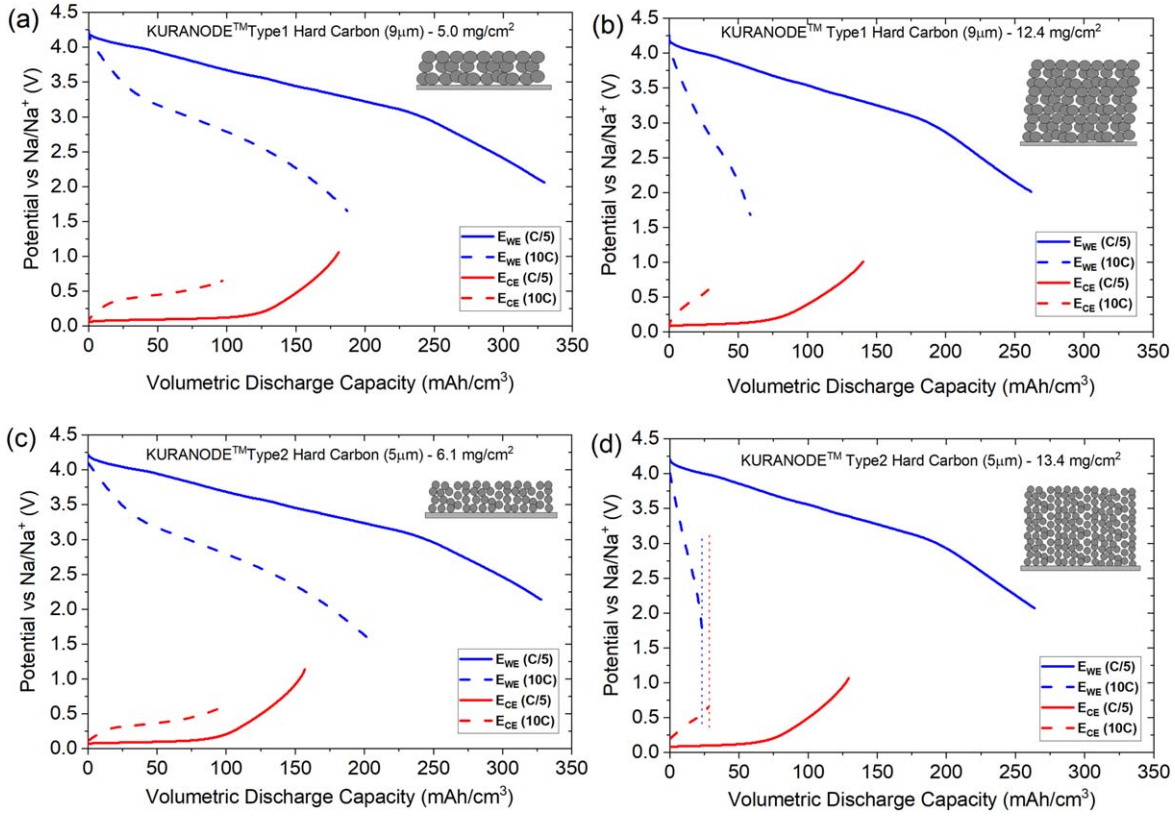

Figure 5. E_{WE} vs Na/Na^+ ($Na_{1-x}Ni_{1-x-y-z}Mg_xMn_yTi_zO_2$ layered oxide cathode in blue) and E_{CE} *vs* Na/Na^+ (hard carbon anode in red) *vs* volumetric discharge capacity (mAh/cm^3) at low and high discharging rates (C/5 and 10 C where 1 C = 130 mA/g_{cath}), denoted by solid and dashed lines respectively. The hard carbon counter electrode is clearly limiting across most conditions in the experimental design apart from the instance of 10 C discharge of the Type2 electrode at 13.4 mg cm^{-2} mass loading (lines have been added to show the limitation of E_{WE}). Volume was taken as the product of electrode thickness minus the current collector thickness and cross-sectional area (2.545 cm^2 based upon an 18 mm^2 disk diameter of three-electrode cells).

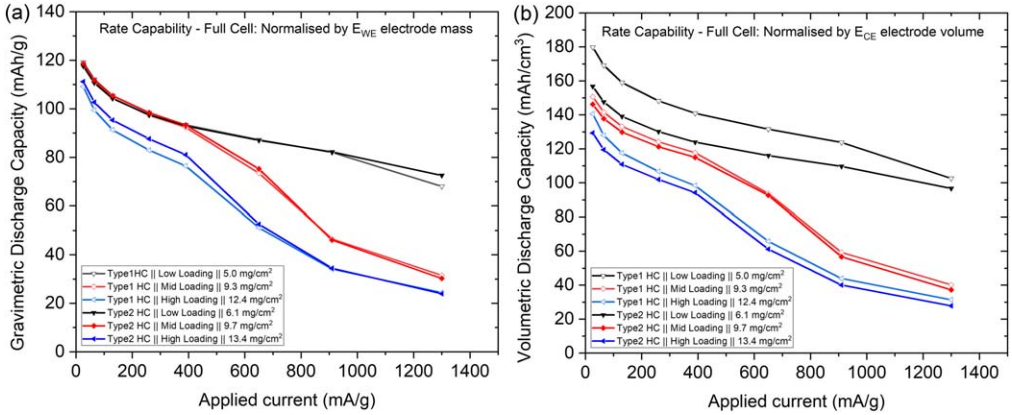

Figure 6. Cell gravimetric and volumetric capacity ($mAh\ g^{-1}$, $mAh\ cm^{-3}$) *vs* applied current ($mA\ g^{-1}$) across three mass loadings and two hard carbon particle sizes. Tests are conducted across a range of current densities from C/5 to 10 C (1 C = 130 $mA\ g^{-1}$). Gravimetric capacity limitation is taken per gram of cathode active material, while volumetric capacity is taken per gram of anode active material as these are proven limiting in the 3-electrode design (see Figs. 5 and 6). Each cell was cycled three times at each applied current, the above points are an average obtained at each applied current level.

different microstructures,[32,33] showing how various pore geometries can cause distortion of the 45° region of the impedance spectra. Pritzl et al. utilised an R/Q element for fitting of graphitic anodes in lithium ion batteries.[19] Through testing EIS responses at various temperatures, they attributed the deviation to contact resistance at the coating/separator interface, thus causing distortions of the 45° region associated with R_{ion}. It is hypothesised that the deviation in 45° region results from a combination of contact resistance at the interface between the electrode and current collector and the resultant pore geometry deviating from the assumed cylindrical shape. In the current work a Q and R/Q elements have been added to symmetrical and three-electrode impedance spectra respectively to account for this phenomenon. In the symmetrical cell configurations this led to excellent chi-squared values ($\sim 10^{-5}-10^{-4}$), compared to use of a simple TLM model by itself ($\sim 10^{-3}$), with the deviation visible in the 45° region.

At low and mid loadings, the HC electrode exhibited an inductive like curve at low frequency in the three-electrode configuration (see Fig. S3). For fitting of the TLM in these instances only values within the positive Z' and Z'' plane was considered. Larger errors in the

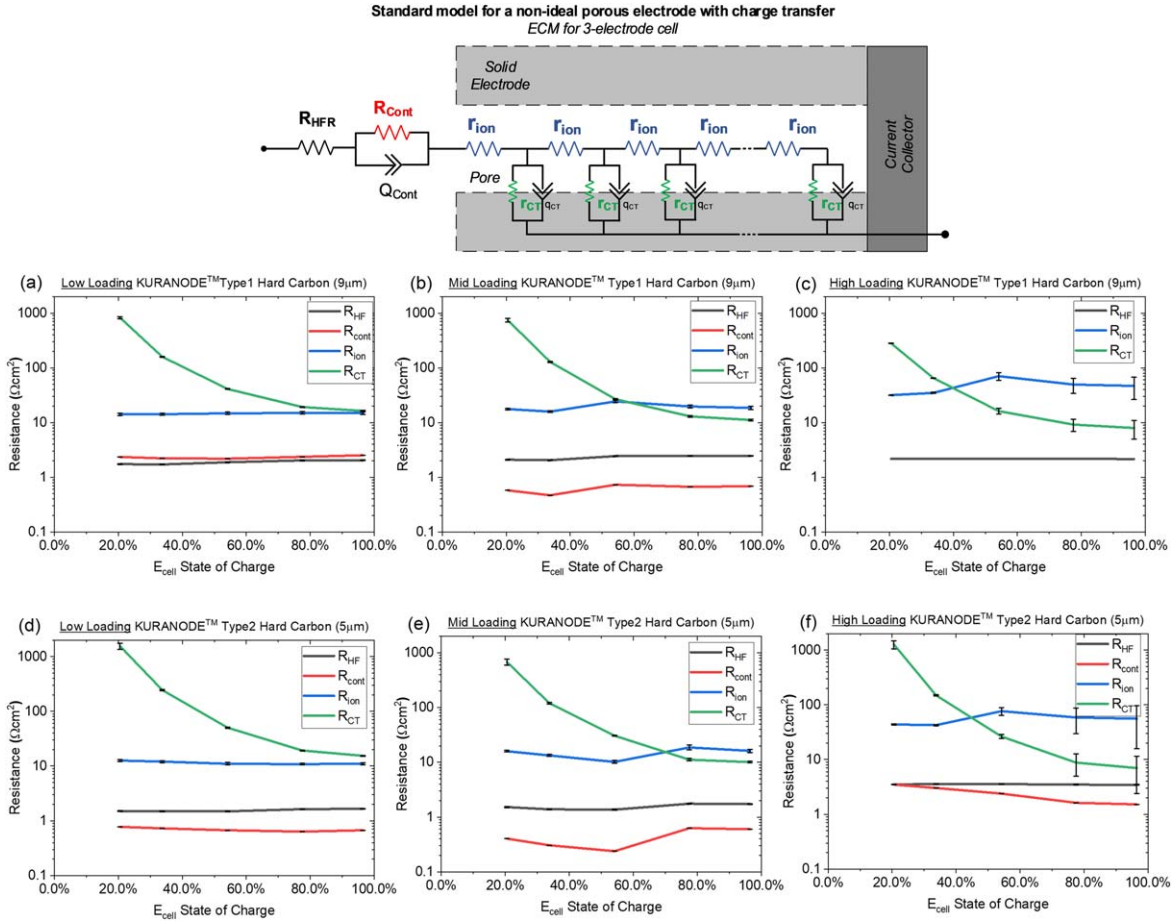

Figure 7. Relative resistance contributions for the hard carbon counter electrode versus sodium reference electrode (Z_{CE} vs Ref) across three mass loadings and two particle sizes. $R_{ion} > R_{CT}$ for the HC electrode at high mass loadings (>9.30 mg cm^{-2}) and high states of charge (E_{cell} > 55%, >∼3 V). At low loadings $R_{ion} < R_{CT}$ across all SOCs for both 5μm and 9μm HC particle sizes. Error bars show the percentage deviation in the elemental fitting.

equivalence circuit fits at high states of charge were attributed to these distortions. Some studies suggest that this artefact may be due to the alignment of the reference electrode and/or influenced by the geometry of the reference electrode type.[34,35] A more recent suggestion for the observed inductive distortion artefact from the test equipment manufacturer is explained by slight bending of the separator near the edges of the cell. This results in a slight distortion of the cell's symmetry leading to inductive type artefacts at low frequencies.

The relative influence of the working electrode has not been considered in this analysis as the response is distorted by the influence of the sodium reference, a common issue associated with trying to analyse sodium-ion cell systems[36,37] (deconvolution of responses can be seen in Fig. S7). To ensure authenticity of the response of the full cell impedance, a separate investigation into two-electrode cell configurations were considered (sodium layered oxide vs hard carbon in CR2032 coin cells). Figure S4 shows an exemplar comparison of three-electrode and two-electrode E_{WE} vs E_{CE} impedance response at various SOC at the high loading level for sodium layered oxide vs Type1 HC full cell. The close match confirms the validity of the experimental approach used for the full cell data recorded in the three-electrode configuration, giving confidence that the sodium reference did not adversely affect the frequency response obtained within this experimental design.

Drawing together the strands of the work, we have observed an increase in R_{ion} value associated with increased thickness in hard carbon symmetrical cells. This increase in R_{ion} is mirrored in full cells as observed through use of a three-electrode EIS study which has been independently verified through comparison to a conventional two-electrode full cell configuration. The three-electrode EIS study illustrated the transition from charge transfer to ionic transport dominant resistance at SOC >50% when areal capacity increases from 1.5 mAh cm^{-2} to 3.2 mAh cm^{-2}. This result is important as it indicates where focus should shift from material to electrode microstructure when developing energy dense cells with improved rate performance.

Consideration also needs to be applied when extrapolating results obtained to other form factors as parameters including temperature and pressure distribution throughout the cell can also influence final rate performance. Faradion have recently released data from 2.5 Ah multi-layer pouch cells revealing capacity retentions in excess of 87% when the cells were discharge at 10 C.[38] Despite the difficulty in translating rate performance data exactly across form factors, improvements in smaller scale cells tend to be reflected in larger form factors, for example as illustrated by Bridgewater et al.[39]

Conclusions

This work has investigated the limiting electrode dynamics within sodium-ion full cells with commercially relevant mass loadings and active materials content. The investigation has shown that the layered oxide electrode is limiting the capacity of the cell gravimetrically (mAh/g) and the hard carbon electrode is limiting volumetrically (mAh/cm^3) upon discharge. By using a three-electrode set-up this was confirmed to be the case for charge rates from C/5 (26 mA g^{-1}) to 10 C (1300 mA g^{-1}) for cathode loadings between 9.6 mg cm^{-2} and 18.5 mg cm^{-2}, with one minor exception (sodium layered oxide limiting at >=1300 mA g^{-1} and 18.5 mg cm^{-2}).

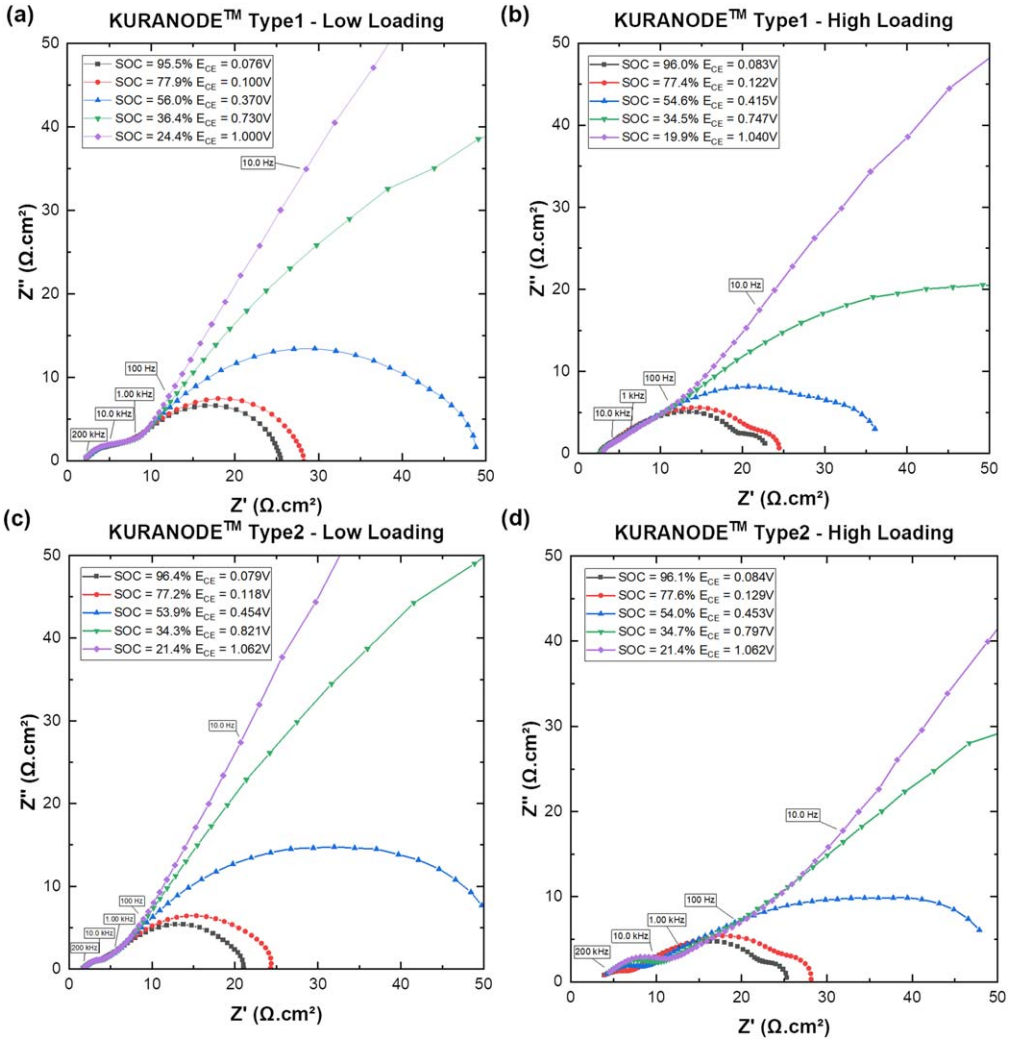

Figure 8. Nyquist plots for the hard carbon counter electrode versus reference electrode (Z_{CE} vs Ref) in three-electrode configuration at five different states of charge across the four corners of the experimental design (high/low loadings of KURANODE™ Type1/Type2 HC electrodes).

Utilising EIS, the evolution of individual resistance contributions has been identified. A TLM has been applied to symmetrical cells in "*blocking*" configuration revealing a linear increase in R_{ion} with mass loading for the HC electrodes tested. Comparatively the sodium layered oxide materials did not exhibit increase in the 45° R_{ion} region. Additionally, an investigation into the trends in cell resistances at various SOCs in "*non-blocking*" conditions was undertaken for the HC electrodes. This revealed $R_{ion} > R_{CT}$ at SOC >∼60%, at the mid loading level and $R_{ion} > R_{CT}$ at SOC >∼50% at the high loading level. Artefacts pertaining to the high and low frequency regions of the EIS spectra were presented with potential explanations of their origins. Finally, full cell impedance responses were validated in the three-electrode PAT-cell configuration by comparing E_{CE} vs E_{WE} Nyquist plots to a two-electrode CR2032 coin cell.

Further work investigating the influence of cathode to anode active material ratio, or the particle shape influence could be interesting future investigations. A similar experimental approach could be used to the current work to allow direct comparison of results.

Acknowledgments

The authors would like to acknowledge the EPSRC Centre for Doctoral Training in Sustainable Materials and Manufacturing (EP/L016389/1) and *Faradion Ltd* for funding this research. IH and CC would also like to thank Ruth Sayers for her feedback and guidance on the manuscript and James Whitley for assisting in electrode fabrication at Faradion.

ORCID

Christopher Constable https://orcid.org/0000-0002-8701-1735
Mark Copley https://orcid.org/0000-0002-6435-8680
Emma Kendrick https://orcid.org/0000-0002-4219-964X
Claire Dancer https://orcid.org/0000-0003-2910-2134
Ivana Hasa https://orcid.org/0000-0002-9099-5464

References

1. N. Tapia-Ruiz et al., *J. Phys.: Energy*, **3**, 031503 (2021).
2. I. Hasa, J. Barker, G. Elia, and S. Passerini, *Reference Module in Chemistry, Molecular Sciences and Chemical Engineering* Sodium Systems | Low Temperature: Overview, (Elsevier) (2023), Ref. Modul. Chem. Mol. Sci. Chem. Eng. 1.
3. I. Hasa et al., *J. Power Sources*, **482**, 228872 (2021).
4. C. Vaalma, D. Buchholz, M. Weil, and S. Passerini, *Nat. Rev. Mater.*, **3**, 18013 (2018).
5. K. G. Gallagher et al., *J. Electrochem. Soc.*, **163**, A138 (2016).
6. R. de Levie and E. Acta, *Electrochimica Acta*, **8**, 751 (1963).
7. J. Bisquert, *Phys. Chem. Chem. Phys.*, **2**, 4185 (2000).
8. N. Ogihara et al., *J. Electrochem. Soc.*, **159**, A1034 (2012).
9. J. Landesfeind, J. Hattendorff, A. Ehrl, W. A. Wall, and H. A. Gasteiger, *J. Electrochem. Soc.*, **163**, 1373 (2016).
10. F. Linsenmann, D. Pritzl, and H. A. Gasteiger, *J. Electrochem. Soc.*, **168**, 010506 (2021).
11. D. I. Iermakova, R. Dugas, M. R. Palacín, and A. Ponrouch, *J. Electrochem. Soc.*, **162**, A7060 (2015).
12. R. Dugas, J. D. Forero-Saboya, and A. Ponrouch, *Chem. Mater.*, **31**, 8613 (2019).
13. X. Chen et al., *Nanoscale*, **11**, 22196 (2019).
14. B. A. Boukamp, *J. Electrochem. Soc.*, **142**, 1885 (1995).
15. M. Schönleber, D. Klotz, and E. Ivers-Tiffée, *Electrochim. Acta*, **131**, 20 (2014).

16. M. Schönleber and E. Ivers-Tiffée, *Electrochem. Commun.*, **58**, 15 (2015).
17. J. Bisquert, G. Garcia-Belmonte, P. Bueno, E. Longo, and L. O. S. Bulhões, *J. Electroanal. Chem.*, **452**, 229 (1998).
18. J. Landesfeind, D. Pritzl, and H. A. Gasteiger, *J. Electrochem. Soc.*, **164**, A1773 (2017).
19. D. Pritzl, J. Landesfeind, S. Solchenbach, and H. A. Gasteiger, *J. Electrochem. Soc.*, **165**, A2145 (2018).
20. N. Ogihara, Y. Itou, T. Sasaki, and Y. Takeuchi, *J. Phys. Chem. C*, **119**, 4612 (2015).
21. W. H. Mulder, J. H. Sluyters, T. Pajkossy, and L. Nyikos, *J. Electroanal. Chem. Interfacial Electrochem.*, **285**, 103 (1990).
22. C. H. Kim, S. Il Pyun, and J. H. Kim, *Electrochim. Acta*, **48**, 3455 (2003).
23. S. M. Rezaei Niya and M. Hoorfar, *Electrochim. Acta*, **188**, 98 (2016).
24. J. B. Jorcin, M. E. Orazem, N. Pébère, and B. Tribollet, *Electrochim. Acta*, **51**, 1473 (2006).
25. A. Kamiyama et al., *ACS Appl. Energy Mater.*, **3**, 135 (2020).
26. H. Zhang, H. Ming, W. Zhang, G. Cao, and Y. Yang, *ACS Appl. Mater. Interfaces*, **9**, 23766 (2017).
27. Q. Meng et al., *ACS Energy Lett.*, **4**, 2608 (2019).
28. Y. Chen et al., *J. Power Sources*, **557**, 232534 (2023).
29. L. Bläubaum et al., *ChemElectroChem*, **7**, 4755 (2020).
30. K. Schutjajew et al., *Phys. Chem. Chem. Phys.*, **23**, 11488 (2021).
31. A. Shodiev et al., *J. Power Sources*, **454**, 227871 (2020).
32. S. J. Cooper, A. Bertei, D. P. Finegan, and N. P. Brandon, *Electrochim. Acta*, **251**, 681 (2017).
33. H. Keiser, K. D. Beccu, and M. A. Gutjahr, *Electrochim. Acta*, **21**, 539 (1976).
34. M. Ender, J. Illig, and E. Ivers-Tiffée, *J. Electrochem. Soc.*, **164**, A71 (2016).
35. R. Raccichini et al., *Batteries*, **5**, 12 (2019).
36. S. E. Lee and M. H. Tang, *J. Electrochem. Soc.*, **166**, A3260 (2019).
37. K. Pfeifer et al., *Chem. Sus. Chem*, **12**, 3312 (2019).
38. R. Sayers, *243rd ECS Meeting*, (Boston, MA) (2023).
39. G. Bridgewater et al., *Batter. 2021*, **7**, 38 (2021).